Materials Advances

ROYAL SOCIETY OF CHEMISTRY

PAPER

View Article Online
View Journal



Cite this: DOI: 10.1039/d6ma00288a

# The influence of tethered dopant templates on the electrochemical, nanomorphological, and nanomechanical properties of 2D conductive polymer films

Luiza A. Nascimento, [abc] Kilian S. Fraysse,[d] Daniel P. Langley,[abc] Rosanne M. Guijt, [e] Paul R. Stoddart, [f] Simon E. Moulton, [fghi] Saimon M. Silva [abc] and George W. Greene *[abc]

Received 3rd March 2026,
Accepted 6th May 2026

DOI: 10.1039/d6ma00288a

rsc.li/materials-advances

Chemical electropolymerization can reliably produce two-dimensional (2D) and ultrathin conductive polymer films but offers limited control over nanomorphology and mechanical stiffness. To address this limitation, we investigate the use of DNA as a tethered dopant template, where the fixed charges of anionic DNA macromolecules grafted onto an electrode are used to dope and finely control electropolymerization in deionized water. The grafted layer adopts distinct conformations and stiffness depending on whether it is single- or double-stranded. Because the chemical composition of the dopant remains unaltered, variations in the resulting conductive polymer films arise solely from differences in the physical properties of the dopant layer. Our findings show that the nanomorphology of the polymer film directly reflects the morphology of the template, and that the dopant enhances mechanical stiffness with minimal impact on electrochemical performance. These results demonstrate that tethered dopant templating is a versatile platform for controlling the conductivity and electrochemical performance of molecularly engineered 2D polymer films, while dopant selection provides a powerful means for manipulating morphological and mechanical properties.



## 1. Introduction

In electropolymerization, polymer growth is inherently coupled to electrochemical charge transfer, ionic transport, and local electric fields, giving rise to a wide range of morphologies, from dense and compact films to highly porous, fibrillar, and cauliflower-like nanostructures. Although deposition parameters can be systematically varied to modify the electrode–electrolyte interfacial environment, the relationships between electrochemical conditions, molecular-scale chain organization, and the resulting morphological and electrochemical properties remain largely empirical.[1] Key structural features such as porosity, grain connectivity, and vertical heterogeneity have a direct impact on conductivity, charge transport, and electrochemical performance; however, these features are strongly coupled to the polymer doping state, oxidation level, and growth history. Consequently, small variations in nucleation behavior, substrate properties, or local mass-transport conditions can lead to significant morphological divergence and limited reproducibility. As a result, performance enhancement is typically achieved through iterative parameter optimization rather than predictive design. The persistent coupling of chemical, mechanical, and transport processes therefore continues to limit precise control, and predictive electrical, electrochemical, mechanical, and morphological properties in electropolymerized polymers remain an outstanding challenge.[2–5]

Tethered dopant templating has emerged as a robust and versatile route to synthesize ultra-thin and two-dimensional conductive polymer films while affording unprecedented control

[a] The Biomedical and Environmental Sensor Technology (BEST) Research Centre, La Trobe Institute for Molecular Science (LIMS), La Trobe University, Melbourne, Victoria 3086, Australia. E-mail: w.greene@latrobe.edu.au
[b] Department of Biochemistry and Chemistry, School of Agriculture, Biomedicine and Environment (SABE), La Trobe University, Melbourne, Victoria 3086, Australia
[c] ARC Research Hub for Molecular Biosensors at Point-of-Use (MOBIUS), La Trobe University, Melbourne, Victoria 3086, Australia
[d] School of Chemistry, Monash University, Clayton, VIC 3800, Australia
[e] Centre for Regional and Rural Futures, Deakin University, Geelong, Victoria 3220, Australia
[f] School of Engineering, Swinburne University of Technology, Melbourne, VIC 3122, Australia
[g] The Aikenhead Centre for Medical Discovery, St Vincent's Hospital Melbourne, Melbourne, VIC 3065, Australia
[h] Iverson Health Innovation Research Institute, Swinburne University of Technology, Melbourne, VIC 3122, Australia
[i] Department of Advanced Components and Materials Engineering, Sunchon National University, 255, Jungang-ro, Suncheon-si, Jellanam-do 57922, Republic of Korea

over composition and fine morphology,[6–8] a capability that derives from three-dimensional spatial regulation of electropolymerization coupled with deliberately slowed reaction kinetics that collectively produce highly repeatable films with uniform thickness and properties across large areas. Tethered dopant templating leverages the critical but often overlooked role of dopant molecules in electropolymerization, which is to stabilize the highly reactive cation radicals formed during monomer oxidation. Without this stabilization the propagation reaction cannot be sustained because chain termination rapidly occurs. By tethering dopant molecules to the electrode surface and performing polymerization in a monomer solution without additional dopants in deionized water, the tethered dopant functions as a template that determines where polymerization occurs and to a significant extent how much polymer can grow. This approach enables precise three-dimensional spatial control of polymer growth and allows the fabrication of ultra-thin, uniform and conformal conductive polymer films.

The 3D-spatial control afforded by tethered dopant templating has been explicitly leveraged to create micro-patterned films by first patterning the tethered dopant on the electrode surface followed by electrochemical polymerization,[6] yielding for example, polypyrrole (PPy) islands that conform to the dopant pattern and demonstrate lithography-grade fidelity in geometry. Beyond single-phase films, the templated growth mechanism has also been used to produce biphasic nanocomposite architectures with nanoscale,[8] interpenetrating phases of PPy and poly(3,4-ethylenedioxythiophene) (PEDOT) by first growing a nanoporous film of one polymer and subsequently growing the second polymer within the pore network of the first. Atomic force microscopy (AFM) phase imaging and electrochemical quartz crystal microbalance (EQCM-D) were used to confirm two distinct phases and a pore-filling evolution, while electrochemical measurements show composite properties that blend those of the constituent homopolymers and can be tuned by adjusting the relative abundance of each phase *via* cycle count and monomer sequence.

The unique process by which conductive polymer films grow in the tethered dopant templating approach, *i.e.*, by initially enveloping the templating dopant molecules followed by progressive infilling, afford a level of compositional control over the final film because the immobilized dopant becomes part of the interfacial nanocomposite and the mass/mole fraction of dopant to polymer can be modulated through the number of polymer growth cycles and the availability of accessible charge sites. Using tethered dopant templating, hyper-doped conductive polymer films have been synthesized with dopant-to-polymer mass fractions far exceeding those achieved by traditional free-dopant electropolymerization, yielding markedly elevated charge-carrier densities and ultra-high conductivities. Two-dimensional PEDOT films prepared with a tethered hyaluronic acid layer[7] exhibit conductivities and charge-transfer kinetics comparable to gold surfaces and display ultra-uniform electrochemical responses down to submicrometer length scales by scanning electrochemical cell microscopy (SECCM) mapping, in stark contrast to the highly inhomogeneous distributions observed in traditionally grown PEDOT films. Collectively these results demonstrate that tethered dopant templating provides precise 3D spatial control, deterministic thickness and morphology programming, micro-patterning capability, phase-engineered composite architectures, and hyper-doped films with superior electrical homogeneity, suggesting a potential broad-based strategy for engineering conductive polymer interfaces with properties that cannot be achieved using conventional synthetic approaches.

So far tethered dopant templating has been successfully demonstrated using two different dopants – lubricin and thiolated hyaluronic acid – which adopt markedly different conformational structures at the electrode interface. Lubricin self-assembles into a well-ordered telechelic polymer brush approximately 100 nanometers thick that is molecularly diffuse, with an average spacing between attachment sites of about nine nanometers. Ppy and PEDOT films grown using lubricin dopants are initially tens of nanometers thick and exhibit a highly nanoporous morphology. In contrast thiolated hyaluronic acid consists of a lower molecular weight chains that attach to gold electrodes through pendant thiol groups forming a molecularly dense loop-and-tail conformation with a thickness of approximately twenty nanometers. Poly(3,4-ethylenedioxythiophene) films grown using thiolated hyaluronic acid dopants are ultra-thin, conformal solid films with 2D, molecular-scale thicknesses (*i.e.*, $<3$ nm). These observations suggest that the structure and nanomorphology of the tethered dopant strongly influence the realized morphology of the conductive polymer film. However, because the chemistries of the two dopants differ substantially, including the nature and density of anionically charged groups, it is not possible to conclude whether these differences arise entirely from structural effects or partially from chemical differences. Furthermore, the envelopment of the dopant by the growing polymer creates a nanocomposite-like structure which raises important questions about how the dopant influences mechanical properties of the resulting film.

The present investigation addresses these questions by introducing DNA as a tethered dopant. DNA offers a unique advantage because it can be engineered into tethered layers that share identical chemical composition while exhibiting vastly different morphological structures and mechanical stiffness. These variations can be achieved by controlling how the DNA is tethered to the electrode surface and by using either single-stranded or double-stranded DNA. This approach provides a systematic platform to decouple structural and electrochemical outcomes that are typically intertwined by chemical effects, enabling evaluation of how dopant architecture influences film morphology and mechanical performance.

## 2. Results

To examine how the tethered dopant layer properties influence the electrochemical and physical characteristics of electrochemically grown PEDOT films, three structurally and mechanically distinct DNA dopant configurations were employed. The first configuration which we refer to as ssDNA consisted of a

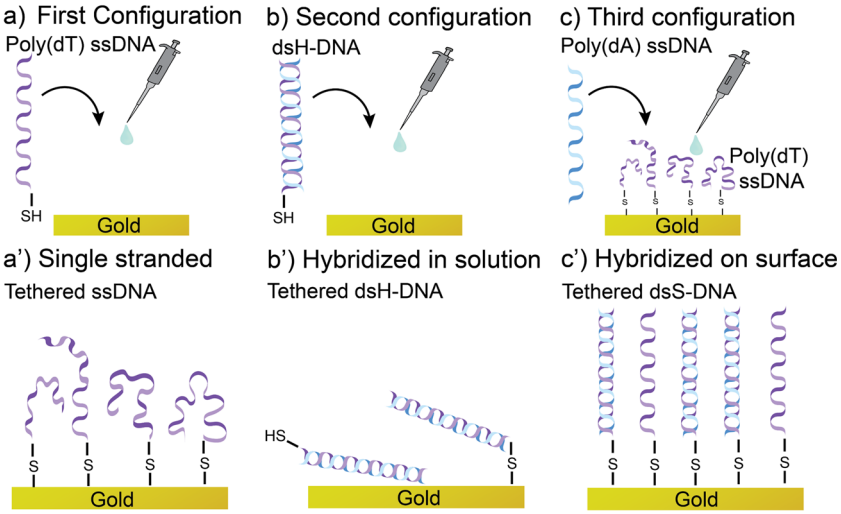


Fig. 1 Graphical representation of the grafting process of (a) ssDNA, and (b) dsH-DNA, when the dsDNA hybridization happens in solution prior to surface grafting and (c) dsS-DNA where hybridization happens on the gold surface. The expected configurations for the tethered layers are represented in (a′), (b′) and (c′) respectively.

50-base single-stranded poly-thymine ($poly(dT)_{50}$) DNA molecule end-grafted to the electrode *via* a single thiol group at the 5′ end (Fig. 1a). With a contour length of approximately 17 nm (assuming ∼0.34 nm per base), this flexible chain exhibits a persistence length of only ∼1.5–2 nm, resulting in a mechanically weak structure that forms a polymer-brush-like layer with semi-extended chains in a mushroom configuration.[9–12] The second configuration, which we refer to as dsH-DNA, involved pre-hybridizing the same $poly(dT)_{50}$ strand with a complementary single stranded poly-adenine ($poly(dA)_{50}$) DNA molecule to form a double-stranded DNA in solution prior to adsorption (Fig. 1b). This double stranded DNA (dsDNA) has a persistence length of ∼50 nm, which is three times the length of the sequence, making it a semi rigid rod with significantly higher mechanical stiffness compared to the single-stranded form. Due to steric hindrance and adsorption from solution, these dsDNA molecules assemble with a low packing density and adopt non-perpendicular orientations relative to the gold surface. The third configuration, which we refer to as dsS-DNA was created by first grafting the single-stranded poly(dT) layer (as in Fig. 1a) and then hybridizing it *in situ* with the complementary strand, producing a dense, close-packed layer of dsDNA oriented predominantly perpendicular to the electrode (Fig. 1c) in a true extended brush configuration.[11,12] This layer retains the same number of grafting sites as the single-stranded layer but close to double the anionic charge density, combining the rigidity of dsDNA from dsH-DNA conformation of Fig. 1b with a markedly different orientation and electrostatic environment.

Oxidation current during electropolymerization is directly related to the amount of monomer oxidized and incorporated into the polymer, as well as the number of charges presented by the grafted dopant layer.[6,7,13] DNA strands, being highly negatively charged and monodisperse, thus exhibit strong electrostatic repulsion during grafting, which introduces excluded-volume effects that influence grafting efficiency and local charge density. These effects become more pronounced with increasing DNA strand length.[14] Although longer ssDNA strands should theoretically yield higher oxidation currents due to greater charge density, this trend is not observed in the voltammograms (Fig. S1), suggesting variations in grafting density likely driven by steric and hydration constraints. The decrease in oxidation current from the first to subsequent CV cycles during 2D PEDOT electropolymerization (Fig. 2a–c) reflects the rapid consumption and envelopment of available dopant charges, causing the reaction to slow significantly with each additional CV cycle. Similarly, while PEDOT doped with dsDNA might be expected to exhibit approximately double the oxidation current than when doped with ssDNA, assuming twice the number of grafted strands and charge sites, the observed current for PEDOT-dsS and -dsH is different between both, and neither is twice that of PEDOT-ss. This discrepancy comes from differences in dsDNA grafting density, confirmed by quartz crystal microbalance with dissipation (Fig. S2), supporting the mechanisms proposed in Fig. 1b′ and c′ for solution *versus* on-surface hybridization.

The 2D conductive polymer produced by tethered dopant templating can achieve hyper-doped states that result in elevated charge-carrier density and mobility that confer exceptionally high conductivity.[7] However, electrode surface morphology and roughness can also potentially influence key electrochemical properties, including conductivity, double-layer capacitance ($C_{dl}$), and charge-transfer resistance ($R_{ct}$). To assess how variations in morphology and roughness of ultra-thin, highly conductive organic films affect electrochemical performance, cyclic voltammetry (CV) and electrochemical impedance spectroscopy (EIS) were conducted in 3.6 mM $K_3[Fe(CN)_6]$ + 3.6 mM $K_4[Fe(CN)_6]$ in 1.0 M KCl (ferro/ferri) aqueous solution electrolyte (Fig. 2d and e). These measurements provide insight into how the electrode interface modulates charge-transfer kinetics and redox reactions, while also revealing intrinsic electrical

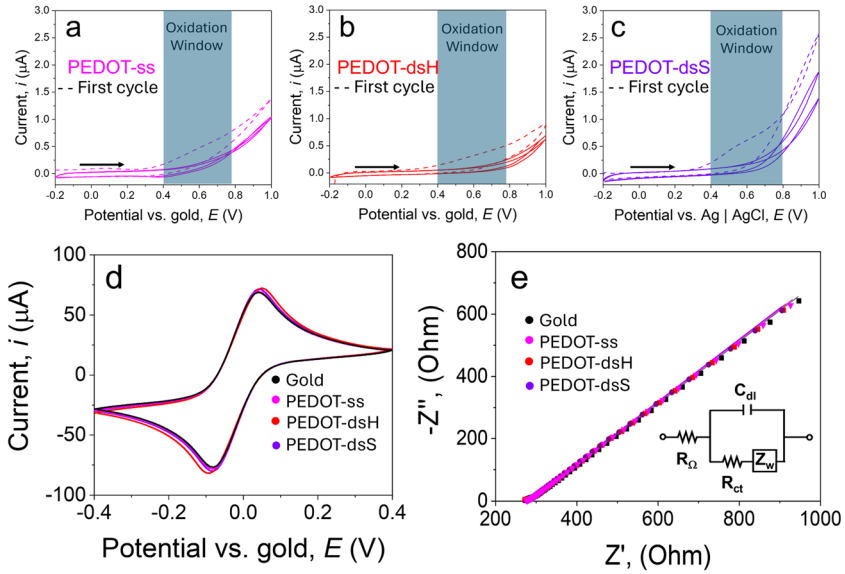


Fig. 2 Cyclic voltammograms for the electropolymerization of EDOT using (a) ssDNA, (b) dsH-DNA and (c) dsS-DNA as tethered dopant templates. Dashed lines represent the first cycle and solid lines represent further cycles, totalizing 3 cycles. Black arrows indicate potential sweep direction. Cyclic voltammograms for 2D-PEDOT doped with different DNA layers in (d) 3.6 mM ferri/ferro in 1.0 M KCl at 50 mV $s^{-1}$ in a potential window of −0.4 V to +0.4 V. (e) EIS in ferri/ferro solution for 2D PEDOT doped with different DNA layers at 0.0 (*vs.* gold) V from $1 \times 10^6$ Hz to 0.1 Hz.

parameters such as $C_{dl}$ and $R_{ct}$. Electropolymerization of 2D PEDOT was performed using the tethered dopant templating approach[6,7] and was carried out by CV scanning from −0.2 V to +1.0 V at 5 mV $s^{-1}$ (*vs.* gold) in 0.01 M 3,4-ethylenedioxythiophene (EDOT) prepared in deionized water. Gold electrodes were modified with different DNA-based dopant layers, including poly(dT)$_{50}$ ssDNA, dsH-DNA, and dsS-DNA. Additional experiments employed ssDNA strands of two other lengths (25 and 100 bases) to modify gold electrodes prior to electropolymerization under identical conditions (see Fig. S1).

While three different tethered DNA dopant structures were used, likely resulting in 2D PEDOT films having some morphological differences, the electrochemical properties of all the films were found to be similar. The redox peak separation ($\Delta E_p$) and peak current magnitudes in the cyclic voltammograms (Fig. 2d) of the 2D PEDOT films are very similar across all three DNA dopant structures and comparable to those of the bare gold electrode, similar to previous 2D PEDOT films grown using tethered hyaluronic acid dopants.[7] This similarity indicates that the specific structure and conformation of the dopant molecules have very little influence over the film's conductivity. Electrochemical impedance spectroscopy was used to calculate $R_{ct}$ and $C_{dl}$ through equivalent circuit modelling. $R_{ct}$ represents the resistance to charge transfer at the interface, while $C_{dl}$ reflects the ability of the surface to store charge and provides additional insight into interfacial charge transfer dynamics. Both parameters were obtained using the Randles circuit as the equivalent model (see Fig. 2e insert) to fit Nyquist plots recorded for 2D PEDOT and gold substrates (Fig. 2e). Average $R_{ct}$ and $C_{dl}$ values are summarized in Table 1 for gold ($n$ = 15), PEDOT-ss, PEDOT-dsH and PEDOT-dsS (all $n$ = 3). Comparable behavior was observed for PEDOT electropolymerized on electrodes grafted with ssDNA of different lengths (see Fig. S3 and Table S1). Overall, the electrochemical performance of 2D PEDOT synthesized using the tethered dopant template approach is similar to metallic gold. In all cases, the polymer reduces $R_{ct}$ by approximately 50 percent relative to gold with minimal changes in $C_{dl}$, demonstrating that the hyper-doped state of the polymer is independent of dopant type and that the resulting films are highly conductive under all conditions.

Table 1 Values of $R_{ct}$ and $C_{dl}$ for gold and 2D PEDOT films doped with tethered ssDNA and dsDNA simulated through Randles circuit from EIS data

| Surfaces | Gold | PEDOT-ss | PEDOT-dsH | PEDOT-dsS |
|---|---|---|---|---|
| $R_{ct}$ (Ohm) | 15.1 ± 4.1 | 7.7 ± 1.2 | 8.8 ± 1.8 | 6.2 ± 0.7 |
| $C_{dl}$ (μF) | 2.5 ± 0.3 | 4.0 ± 1.0 | 1.2 ± 0.03 | 3.6 ± 0.7 |

The CV and EIS characterizations of the differently doped 2D PEDOT films indicate that the electrochemical properties of the films do not appear to be significantly affected by the specific molecular architecture of the tethered dopant layers, despite clear differences in dopant molecule density and overall charge density. During the tethered-dopant templating process, electropolymerization produces PEDOT films that initially exist in a hyper-doped state because the growing polymer incorporates a very high mole fraction of dopant when the film thickness is still minimal. As a result, the electrochemical properties of the final films are largely insensitive to whether the dopant layer adopts a flexible single-stranded configuration, a loosely packed double-stranded arrangement, or a densely packed perpendicular orientation. However, the measured values of $R_{ct}$ and $C_{dl}$, while broadly similar across all architectures, exhibit a slight trend in which $R_{ct}$ decreases modestly as the density of DNA

molecules and the corresponding anionic charge density increase. These observations indicate that the electrochemical behavior of 2D PEDOT films is governed primarily by the hyper-doping effect, which arises from the control exerted by the tethered dopant template during electropolymerization. The amount of polymer deposited is limited by the initial charge density of the dopant layer, leading to a high dopant-to-polymer ratio and promoting the formation of long polymer chains. Additional characterization using CV and EIS for 2D PEDOT films doped with layers of varying ssDNA lengths (Fig. S3) confirms this trend, as similar electrochemical behavior is observed across all cases (Table S1).

While the specific architecture adopted by the dopant does not appear to significantly influence electrochemical properties, AFM imaging studies were carried out to investigate the resulting morphological effects. To investigate how changes in dopant layer morphology influence polymer nanostructure, atomic force microscopy (AFM) topography and phase images were acquired for the 2D PEDOT films. Topography scans are presented as both 2D and 3D renderings to enhance visualization of surface depth and spatial features. AFM phase images represent variations in energy dissipation between the probe and the sample surface, which correlate with local mechanical properties such as stiffness and viscoelasticity.[15] The phase images thus visualize compositional and/or structural heterogeneity at the nanoscale.

For PEDOT-ss (Fig. 3a and a′), the topography reveals rounded asperities with minimal structural organization, consistent with a dopant layer formed by end-grafted random coils of ssDNA in a 'blobby' mushroom configuration. The phase image (Fig. 3a″) further emphasizes the absence of well-defined asperity shapes, indicating a higher uniformity in mechanical properties than suggested by topography alone. Overall, the 2D PEDOT film exhibits near-uniform stiffness, as evidenced by minimal phase-shift variation across the scanned area. 2D PEDOT films synthesized using ssDNA of different length (*i.e.*, base number) were also imaged with AFM and shown in Fig. S4 of the SI. All these 2D PEDOT films exhibit very similar morphologies and uniform mechanical properties regardless of ssDNA length. Quantitative roughness metrics including RMS and Peak-to-Valley (P–V) values are provided in Table S2 as well as the predicted ssDNA layer conformations which are shown in Fig. S3a‴–b‴ of the SI.

The AFM analysis of PEDOT-dsH films (Fig. 3b and b″) confirms that the polymer forms a continuous layer across the substrate. Within this film, the topography reveals a distinct texture that appears as an intricate, interconnected nanoscale ridge-valley network structure. This network becomes even more apparent in the phase image (Fig. 3b″), where it correlates with pronounced mechanical heterogeneity across the surface. Such heterogeneity arises from the sharp contrast between the relatively soft PEDOT matrix and the mechanically stiff dsDNA molecules. Due to the low grafting density, dsDNA strands are expected to adopt a more perpendicular orientation

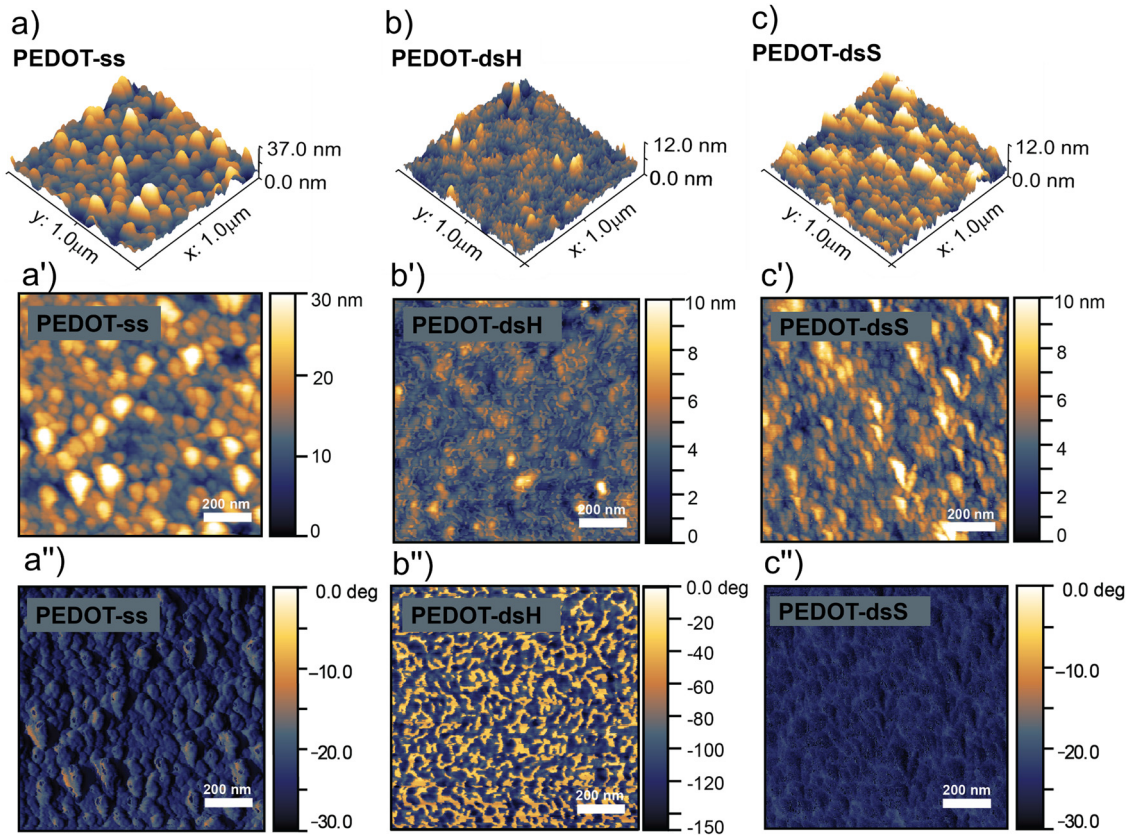


Fig. 3 3D representation of the AFM topography scan for (a) PEDOT-ss, (b) PEDOT-dsH and (c) PEDOT-dsS rotated at $\varphi$ = 45 and $\theta$ = −45. 2D representation of the AFM topography scan for (a′) PEDOT-ss, (b′) PEDOT-dsH and (c′) PEDOT-dsS and respective phase images (a″), (b″) and (c″).

relative to the gold surface. In this configuration, the stiffness of the dsDNA resists bending during lateral AFM tip scanning, causing these regions to appear as well-defined bright areas in the phase image. Interestingly, the dimensions of these stiff regions far exceed the contour length of a single dsDNA molecule (~17 nm), implying that individual strands aggregate into larger clusters during PEDOT electropolymerization in a process analogous to fiber pilling. This aggregation mechanism explains the network morphology observed in AFM images. Furthermore, such clustering behavior provides insight into similarly structured nanoporous PPy films synthesized using molecularly diffuse lubricin dopant layers, which share comparable characteristics of low grafting density and large intermolecular spacing.[8]

In the PEDOT-dsS, where the dsDNA hybridization was performed following the end-grafting of ssDNA (Fig. 3c), the resulting nanomorphology differs significantly from that of PEDOT-dsH, where pre-hybridized dsDNA was grafted from solution. Unlike the interconnected nanoscale ridge-valley network structure observed for PEDOT-dsH (Fig. 3b′), PEDOT-dsS exhibits a more randomly rough architecture similar to the PEDOT-ss (Fig. 3a′) but with smaller and more uniformly sized asperities (Fig. 3c′). The topography image of PEDOT-dsS (Fig. 3c′) reveals circular to oval-shaped asperities consistent with the envelopment of brush-like dopant layer of upright rods. In contrast to the PEDOT-dsH, the phase image for PEDOT-dsS (Fig. 3c″) displays a highly uniform surface, devoid of pores, supporting the interpretation of a densely packed dopant layer. In the upright orientation, the dsDNAs are unable to interact strongly with the scanning AFM tip so little mechanical variation is observed in the film's surface.

RMS and P–V roughness values (Table 2) for the different 2D PEDOT films were calculated using the image processing software Gwyddion (version 2.66). PEDOT-ss exhibits the highest RMS roughness, approximately 5.3 nm, which reflects its random coil conformation of end-grafted ssDNA in a mushroom-like configuration. This interpretation is supported by the fact that the RMS value is only slightly greater than the expected hydrodynamic radius of 2–3 nm for a 50-base ssDNA strand under physiological salt conditions.[16] The similarity between RMS and P–V roughness for PEDOT-ss suggests that the surface asperities have a roughly hemispherical morphology again supporting the influence of the random coil conformation of the ssDNA dopant on the final film morphology.

To ascertain the thickness of the PEDOT films, contact mode topography scans at the edge of the polymer were taken to register the step difference between the polymer film and the underlying gold electrode. To facilitate the localization of the polymer edge, a gold coated glass slide was masked using a dye punched silicone-free adhesive film prior to dopant tethering. Topography scans of the step height were also taken for the ssDNA and dsH-DNA layers. However, the step topography images for both DNA layers (Fig. S4a and b) show edge effects. These edge effects are a consequence of the drop-casting tethering approach being made after the electrode is masked, causing a liquid–solid-air interface, *i.e.* three-phase boundary, that results in irregular tethering.[17] For that reason, the precise thickness of the polymers were not established, however, the topography images (Fig. S4c and d) and height traces highlight that the films are all thinner than 10 nm (Fig. S4c′ and d′), and PEDOT-dsH is significantly thinner than PEDOT-ss, and the resulting polymer films are uniform and conformal with the grafting density of the corresponding DNA layers.

The phase images (Fig. 3a″–c″) for 2D PEDOT suggest that the mechanical properties of the films vary depending on the dopant layer, with dsDNA-containing films appearing mechanically stiffer. However, phase contrast can also be influenced by other factors such as surface adhesion or friction, making it unsuitable for quantitative analysis. This limitation justifies the need for direct force measurements to accurately determine mechanical properties.

To confirm that the incorporation of mechanically stiff dsDNA dopant results in mechanically stiffer PEDOT films compared with the ssDNA doped PEDOT, force–distance measurements were performed, and Young's modulus was calculated using the Derjaguin–Muller–Toporov (DMT) model. The DMT model assumes that the contact radius and indentation depth are small compared to the sample thickness, which is a reasonable approximation for bulk materials. However, because the 2D PEDOT films are extremely thin, this assumption does not hold. Consequently, the Young's modulus values derived from DMT modeling do not represent the true modulus of these films. Instead, the DMT analysis provides a qualitative comparison of relative stiffness between samples.[18]

Each force curve was fitted to the DMT model, and the resulting histograms and distribution curves for the tethered ssDNA (before polymerization), PEDOT-ss, tethered dsDNA (hybridized in solution), and PEDOT-dsH are shown in Fig. 4a and b. Normal force measurements were first performed on the tethered dopant layers prior to electropolymerization, revealing an increase in the apparent Young's modulus from approximately 263 MPa for ssDNA to about 332 MPa for dsDNA (Fig. 4a), consistent with the inherently higher stiffness of dsDNA.

Normal force measurements were next performed on PEDOT-ss and PEDOT-dsH films (Fig. 4b), confirming the same trend observed for the tethered dopants prior to polymerization. After electropolymerization, PEDOT-dsH shows a significantly broader range of modulus values compared to PEDOT-ss, likely reflecting the biphasic distribution of mechanical properties observed in the phase image. In addition, PEDOT-dsH exhibited an apparent Young's modulus roughly two times higher than PEDOT-ss, providing strong evidence that the enveloped dopant substantially reinforces the polymer film. This reinforcement effect is analogous to the role of glass or carbon fibers in composite materials, where rigid inclusions enhance overall mechanical strength.

Table 2 Statistical values on the different 2D PEDOT surfaces calculated from the AFM images

| Surfaces | PEDOT-ss | PEDOT-dsH | PEDOT-dsS |
|---|---|---|---|
| RMS roughness (nm) | 5.3 | 1.1 | 1.8 |
| Peak-valley roughness (nm) | 5.1 | 4.1 | 5.0 |

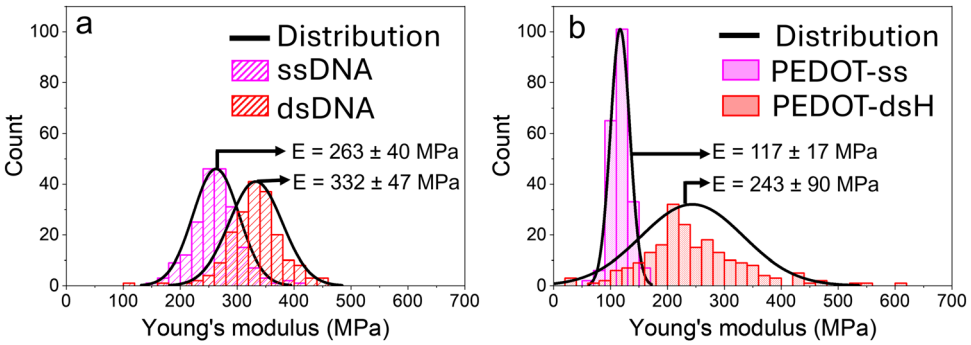


Fig. 4 Histograms of the Young's modulus for (a) ssDNA and dsDNA and (b) PEDOT-ss and PEDOT-dsH. The black curves are the distribution curves for each histogram.

# 3. Conclusion

The tethered dopant templating approach not only enables the fabrication of highly conductive 2D polymers with precise control over electropolymerization and doping levels but also dictates the resulting material's mechanical and morphological properties. This strategy achieves a hyper-doped state that is independent of dopant choice because it maximizes the intramolecular interfacial area, regardless of the tethered dopant layer morphology. As a result, electrochemical and electrical properties such as $R_{ct}$ and $C_{dl}$ remain very low, which is consistent with highly conductive materials, and can even improve compared to the underlying substrate. Importantly, this decoupling means that morphology and mechanical strength can be tailored simply by selecting dopants with desired structural and mechanical characteristics, without compromising electrical performance.

Traditionally, morphology and mechanical properties influence electrochemical behavior; however, with tethered dopant templating, this correlation is eliminated. The approach intrinsically produces highly conductive 2D polymers independent of dopant selection, while the dopant layer serves as a template for defining morphology and mechanical properties.

Beyond electrochemical performance, the ability to control morphology and mechanical properties is critical for applications such as optimizing electrode–tissue interfaces for neuroimplants and drug delivery systems,[19,20] enabling precise polymer actuation for controlled release,[21] and designing scaffolds for tissue engineering.[22,23] The tethered dopant templating approach provides a robust and scalable platform for engineering 2D conductive polymers with finely tuned morphology and mechanical properties, offering new opportunities for advanced biomedical and electronic applications.

# 4. Methods and materials

## 4.1. Chemicals

3,4-Ethylenedioxythiophene (EDOT), potassium chloride (KCl), potassium ferricyanide III ($K_3[Fe(CN)_6]$), potassium ferrocyanide IV ($K_4[Fe(CN)_6]$), tris(2-carboxyethil)phosphine (TCEP), and phosphate buffered saline tablets (PBS) from Sigma-Aldrich (Castle Hill, Australia), thiolated DNA from Integrated DNA Technologies (Sydney, Australia).

## 4.2. DNA grafting

The substrates used as electrodes for DNA grafting and electropolymerization were laser scribed three electrode system gold polymer webs (Universal Biosensors - UBI). The electrodes were used as is, with no previous cleaning or pre-treatment as it is purchased with a protective plastic layer that was removed immediately before modification with DNA grafted layer.

DNA solutions were prepared at 1 mM in PBS and TCEP was added to a concentration of 100 mM to reduce any unwanted disulfide bonds along the DNA chains. The DNA solution with TCEP was left to react for 1 h at room temperature (25 °C). Grafting of the DNA dopant layer on the gold electrodes was performed by drop casting the reduced 1 mM solution of the DNA in PBS and left incubating for 30 min at room temperature before rinsing with Mili-Q water and drying under $N_2$ flow prior to their use in electropolymerization.

To assess the impact of different dopant layer morphologies in the resulting polymer film, different DNA chain lengths and structures were grafted. Poly(dT) DNA strands with lengths of 25, 50 and 100 bases were grafted, as well as dsDNA with 50 bases pairs, hybridized in solution and on the surface. For hybridization in solution, dsH, thiolated poly(dT) and non-thiolated poly(dA) sequence were mixed in the same PBS solution to final concentration of 1 mM each and left hybridizing for an hour in the presence of 100 mM TCEP. For the hybridization done on the electrode surface, dsS, single stranded thiolated poly(dT) sequence was grafted on the gold electrode following the ssDNA grafting procedure; after rising and drying, the electrode was incubated in the reduced non-thiolated poly(dA) sequence solution in PBS at 1 Mm for 30 minutes before rinsing in DI water and drying in $N_2$ flow.

## 4.3. Electropolymerization

Ultra-thin PEDOT films were electropolymerized using a tethered dopant template method adapted from Desrosches *et al.*[6] Electropolymerization was performed through CV in 0.01 M EDOT solution in DI water over gold electrodes modified with a grafted layer of thiolated ssDNA in different chain lengths (25, 50 and 100 bases) and different configurations of dsDNA

(dsH and dsS). Electropolymerization CV was carried out using a scan rate of 5 mV $s^{-1}$, a potential window of −0.2 V to +1.0 V *versus* gold for 3 cycles using a *Multi*PalmSens4 Potentiostat/Galvanostat/Impedance Analyzer (PalmSens).

### 4.4. Electrochemical characterization

The electrochemical properties of synthesized PEDOT films were characterized using two different electrochemical techniques, CV and EIS, carried out using a *Multi*PalmSens4 Potentiostat/Galvanostat/Impedance Analyzer (PalmSens).

To evaluate the intrinsic electrochemical characteristics of the different PEDOT films, CV characterization was carried out in PBS (pH 7.4, 10 mM phosphate buffer, 140 mM NaCl). To evaluate the PEDOT film charge transfer characteristics, CV characterization on the same films was also performed in 3.6 mM $K_3[Fe(CN)_6]$/3.6 mM $K_4[Fe(CN)_6]$ in 1.0 M KCl (ferro/ferri) aqueous solution. All CVs were performed using a scan rate of 50 mV $s^{-1}$ and a potential window −0.4 V to +0.4 V.

Further analysis of the electrical properties of the 2D PEDOT films was obtained using EIS. To ascertain the values of $R_{ct}$ and $C_{dl}$, EIS was also performed on the 2D PEDOT films in ferro/ferri solutions and the recorded Nyquist plots were fitted using the Randles' equivalent circuit model. EIS was carried out at 0.0 V (*vs.* gold) at a frequency ranging from 1 MHz to 0.1 Hz. The data was fitted to the equivalent circuit model using the PalmSens MultiTrace 4.5 software. The average $R_{ct}$ and $C_{dl}$ were obtained from a triplicate for all cases.

### 4.5. AFM imaging

The nanomorphology of the PEDOT doped with ssDNA and dsDNA tethered template were characterized using an NT-MDT AFM. High resolution images of the PEDOT film's nanomorphology were obtained using tapping mode in air and antimony doped silicon AFM tips (model ACT-10; AppNano) with a nominal tip radius <10 nm and a nominal spring constant of 13–77 N $m^{-1}$.

Nanomorphology images were processed using the software Gwyddion (version 2.66). The average root-mean-square (aRMS) and P–V RMS were obtained through the statistical quantities feature on the same processing software, using 512 scan lines.

To investigate PEDOT thickness, step-height topography scans of the ssDNA and dsH-DNA layers, as well as the correspondent PEDOT films were collected in a JPK Nanowizard Sense AFM, in contact mode using a 240AC-NA cantilever in air. The images were processed in Gwyddion (version 2.66), and height traces were collected from four different lines across the scan area, getting the step height difference between the gold substrate and the PEDOT film. The traces were averaged to obtain a representative step height trace.

### 4.6. Force measurements

Prior to any force work measurement, the cantilever spring constant and sensitivity were calibrated using a contact-based method *i.e.*, sensitivity was assessed in air *via* a force-distance measurement against a clean fused silica surface; then the linear portion of the separation curve was fitted and the slope (sensitivity) obtained. The AFM tip was then disengaged and lifted from the surface (by a few micrometers). The spring constant was determined by using the thermal method (*i.e.*, free fluctuations of the cantilever).

The tip radius was measured before each force - work measurement (*i.e.*, each time the sample was changed) by imaging a calibration grating (TGT1, Nanotechnology Solutions) (silicon wafer surface consisting of a 3D array of sharp tips, nominal height 300 – 500 nm and radius of curvature <10 ~ nm). For the measurement, the TGT1 surface was imaged in contact mode, and the apex of each tip was fitted with a spherical/circular model.

The force measurements were collected, and each force-distance curve was fitted using the Derjaguin–Muller–Toropov (DMT) model, given the adhesive nature of the contact between the probe and the sample. Also, given the small forces used, the contact was assumed spherical.

### 4.7. Quartz crystal microbalance with dissipation (QCM-D)

To obtain information on the grafting density of dsH-DNA and dsS-DNA, the grafting of each configuration was carried out in a QSense Analyser (Biolin Scientific). To ensure that the sensor surface would be saturated with DNA in both configurations, the sensors were previously cleaned with basic piranha solution (1 : 1 : 3 ammonia : hydrogen peroxide : Mili-Q water) for 20 min under heating at 80 °C in a hot plate, then thoroughly rinsed with Mili-Q water and dried under nitrogen flow.

Prior to the grafting, absolute ethanol was flushed into the system with a peristaltic pump to remove any possible air bubbles. After that, PBS was pumped at 100 μL $min^{-1}$ to establish a frequency and dissipation baseline in the QSense QSoft401 software. Once the PBS baseline was stable, the grafting for both configurations was carried as described below.

For dsS-DNA, a 1 mM solution of thiolated poly(dT), after TCEP protocol (see Section 6.2), was pumped at 100 μL $min^{-1}$. After a frequency shift was observed, the solution was left incubating for 30 minutes in stationary conditions. After incubation, PBS was pumped at 100 μL $min^{-1}$ for five minutes to mimic the rinsing step in Section 6.2 followed by pumping 1 mM poly(dA) solution and left incubating for 30 minutes in stationary conditions. Due to the small volume of the QCM-D chambers, the poly(dA) solution was pumped and incubated again to ensure that the hybridization was complete.

For dsH-DNA, the poly(dT) and poly(dA) chains were hybridized as described in Section 6.2 and pumped into the QCM-D chamber after establishing a PBS baseline. Once a frequency shift was observed, the dsH-DNA solution was left incubating for 30 min in stationary conditions, but with short successive pumps to ensure saturation of the QCM-D crystal.

Both configurations were measured in triplicates and a representative averaged curved was obtained.

## Author contributions

Luiza A. Nascimento: investigation, methodology, writing – original draft, writing – review and editing, data curation, formal analysis. Kilian S. Fraysse: writing – review and editing,

investigation, resources, methodology. Daniel P. Langley: writing – review and editing. Rosanne Guijt: writing – review and editing, supervision. Paul R. Stoddart: writing – review and editing, supervision. Simon Moulton: writing – review and editing, supervision. Saimon M. Silva: writing – review and editing, supervision, conceptualization, methodology. George W. Greene: writing – review and editing, supervision, conceptualization, methodology, funding acquisition.

## Conflicts of interest

George W. Greene, Saimon M. Silva and Simon E. Moulton are the inventors on a patent application for the surface tethered dopant templating method assigned to a third party.

## Data availability

The data supporting this article has been included as part of the supplementary information (SI). Supplementary information: Electropolymerization voltammograms for PEDOT-25 and PEDOT-100, QCM-D for dsS-DNA and dsH-DNA grafting, CV and EIS in ferro/ferri for PEDOT-25 and PEDOT-100, topography and phase AFM scans for PEDOT-25 and PEDOT-100 as well as calculated $R_{ct}$, $C_{dl}$, RMS and P–V roughness for PEDOT-25 and PEDOT-100. Unprocessed data will be made available upon reasonable request to the corresponding author. See DOI: https://doi.org/10.1039/d6ma00288a.

## Acknowledgements

This work was partially supported by internal start-up funding provided by La Trobe University and the ARC Industrial Transformation Research Hub (IH240100013). Part of this work was performed at IFM. L. A. N is supported by an Australian Government Research Training Program Scholarship.

## References

1 H. Mousavi, L. M. Ferrari, A. Whiteley and E. Ismailova, *Adv. Electron. Mater.*, 2023, DOI: 10.1002/aelm.202201282.
2 A. Cetinkaya, M. A. Unal, H. Nazır, M. E. Çorman, L. Uzun and S. A. Ozkan, *Microchim. Acta*, 2024, **191**, 270.
3 B. Zhao and P. Wilson, *Polym. Chem.*, 2023, **14**, 2000–2021.
4 Y. Ren and Y. Xu, *Chem. Soc. Rev.*, 2024, **53**, 1823–1869.
5 D. Pham, R. Gouafong, J. Irvin, B. McKinney, J. Dileonardi, M. Cox and A. Aphale, *Sci. Rep.*, 2026, **16**, 11720.
6 P. E. Desroches, K. S. Fraysse, S. M. Silva, K. Firipis, A. Merenda, M. Han, L. F. Dumée, A. F. Quigley, M. I. R. Kapsa, C. D. O'Connel, S. E. Moulton and G. W. Greene, *Electrochim. Acta*, 2023, **463**, 142817.
7 L. A. Nascimento, K. S. Fraysse, K. Krause, C. L. Bentley, M. Han, R. M. Guijt, P. R. Stoddart, S. Moulton, S. M. Silva and G. W. Greene, *ACS Appl. Mater. Interfaces*, 2025, 45042–45055.
8 P. E. Desroches, K. S. Fraysse, A. F. Quigley, R. M. I. Kapsa, L. A. Do Nascimento, S. E. Moulton, M. Han, S. M. Silva and G. W. Greene, *Electrochim. Acta*, 2024, **489**, 144227.
9 J. Aymami, M. Coll, C. A. Frederick, A. H.-J. Wang and A. Rich, *Nucleic Acids Res.*, 1989, **17**, 3229–3245.
10 K. Wang, C. Goyer, A. Anne and C. Demaille, *J. Phys. Chem. B*, 2007, **111**, 6051–6058.
11 A. Opdahl, D. Y. Petrovykh, H. Kimura-Suda, M. J. Tarlov and L. J. Whitman, *Proc. Natl. Acad. Sci. U. S. A.*, 2007, **104**, 9–14.
12 E. Pyrak, A. Jaworska and A. Kudelski, *Molecules*, 2019, **24**, 3921.
13 A. J. Bard, L. R. Faulkner and H. S. White, *Electrochemical methods: fundamentals and applications*, John Wiley & Sons, Ltd., 3rd edn, 2022, 1–17.
14 J. N. Israelachvili, *Intermolecular and Surface Forces*, Elsevier, Santa Barbara, 3rd edn, 2011, pp. 381–410.
15 M. Stark, C. Möller, D. J. Müller and R. Guckenberger, *Biophys. J.*, 2001, **80**, 3009–3018.
16 S. Doose, H. Barsch and M. Sauer, *Biophys. J.*, 2007, **93**, 1224–1234.
17 J. N. Israelachvili, *Intermolecular and Surface Forces*, Elsevier Inc., Santa Barbara, 3rd edn, 2011, pp. 451–460.
18 H. Long, H. Lin, S. Li, Y. Bai, L. Qin, T. Xiao and A. Qin, *Appl. Surf. Sci.*, 2022, **590**, 153126.
19 M. R. Abidian, K. A. Ludwig, T. C. Marzullo, D. C. Martin and D. R. Kipke, *Adv. Mater.*, 2009, **21**, 3764–3770.
20 M. R. Abidian, D.-H. Kim and D. C. Martin, *Adv. Mater.*, 2006, **18**, 405–409.
21 C. Wischke, M. Behl and A. Lendlein, *Expert Opin. Drug Delivery*, 2013, **10**, 1193–1205.
22 K. Namsheer, V. B. Reneesha and C. S. Rout, *ACS Symp. Ser.*, 2023, **1438**, 9–27.
23 M. Khan, M. F. A. D. Refati, M. M. R. Arup, Md. A. Islam and M. H. Mobarak, *Adv. Polym. Technol.*, 2025, DOI: 10.1155/adv/4234491.